nuclear fusion
IAEA

PAPER • OPEN ACCESS

Magnetic geometry effects on turbulent density fluctuations in Wendelstein 7-X

To cite this article: J.-P. Bähner *et al* 2026 *Nucl. Fusion* **66** 016007

OPEN ACCESS
IOP Publishing | International Atomic Energy Agency
Nuclear Fusion
Nucl. Fusion **66** (2026) 016007 (17pp)
https://doi.org/10.1088/1741-4326/ae15a3

Magnetic geometry effects on turbulent density fluctuations in Wendelstein 7-X

J.-P. Bähner[1,2,*], L. Podavini[2], A. Bañón Navarro[3], M. Porkolab[1], S.K. Hansen[1], E.M. Edlund[4], A. von Stechow[2], S.A. Bozhenkov[2], O.P. Ford[2], G. Fuchert[2], F. Jenko[3], A. Langenberg[2], N.A. Pablant[5], E. Pasch[2], P.Zs. Pölöskei[2], T. Romba[2], A. Zocco[2], O. Grulke[2,6] and the W7-X Team[2,a]

[1] MIT Plasma Science and Fusion Center, Cambridge, MA 02139, United States of America
[2] Max Planck Institute for Plasma Physics, 17491 Greifswald, Germany
[3] Max Planck Institute for Plasma Physics, 85748 Garching, Germany
[4] SUNY Cortland, Cortland, NY 13045, United States of America
[5] Princeton Plasma Physics Laboratory, Princeton, NJ 08540, United States of America
[6] Technical University of Denmark, 2800 Kongens Lyngby, Denmark

E-mail: jpbahner@mit.edu

Received 23 April 2025, revised 14 October 2025
Accepted for publication 21 October 2025
Published 3 November 2025

Abstract

Line-integrated density fluctuation measurements from the core of the optimised stellarator Wendelstein 7-X (W7-X) are studied in the context of magnetic field geometry changes. The amplitude as well as the spectral distribution of fluctuations is affected by varying the magnetic field configuration. Weaker turbulent fluctuations are observed in configurations with higher rotational transform and lower magnetic mirror depth. Simulations with the gyrokinetic codes `stella` and GENE-3D are used to investigate the role of magnetic geometry for the experimental observations. The stabilising effect of the high rational transform configuration is reproduced by simulations and can be associated with stronger shaping of the magnetic field. This leads to increased finite Larmor radius and local shear effects, which limit the toroidal extent of ion temperature gradient (ITG) modes. For W7-X configurations with higher magnetic mirror depth, gyrokinetic theory and simulations predict weaker fluctuations, since they are closer to having the maximum-J property, which has a stabilising effect on trapped-electron mode and ITG. The opposite trend is observed experimentally, which can therefore not be explained by geometry effects on turbulence alone.

Keywords: plasma turbulence, stellarator, Wendelstein-7X, optimisation

(Some figures may appear in colour only in the online journal)

[a] See Grulke *et al* 2024 (https://doi.org/10.1088/1741-4326/ad2f4d) for the W7-X Team.
[*] Author to whom any correspondence should be addressed.

1. Introduction

Optimised stellarator experiments such as Wendelstein 7-X (W7-X) demonstrate the successful reduction of neoclassical transport through optimising the magnetic field geometry [1]. In turn, the confinement behaviour of W7-X is dominated by turbulent transport [2, 3] and research on stellarator optimisation now moves towards turbulence-optimised configurations for future stellarator reactors. To optimise for reduced turbulent transport, metrics and models are being developed exploring the effects of magnetic geometry on turbulence drive and saturation [4, 5]. The experimental assessment of these effects, however, is challenging since it requires a stellarator device with sufficient neoclassical optimisation to be in a turbulence dominated, yet reactor-relevant confinement regime. Furthermore, a variable magnetic field configuration and extensive turbulence diagnostic capabilities are required. Currently, W7-X is the only device in operation that offers these unique experimental conditions. The variability of the magnetic field configuration in W7-X is limited, i.e. the current set of coils cannot produce turbulence optimised configurations which usually need a special coil design. However, it can be used to explore the impact of geometry changes within the configuration space of W7-X on the experimentally measured turbulent fluctuations and overall confinement. Previous studies in matched profile experiments already found a beneficial effect of certain magnetic configurations on anomalous electron heat transport in the inner half of the plasma originating from electron-scale turbulence [6]. In this work, we show robust differences in measured turbulent fluctuations at the ion scale across the W7-X configuration space in a database approach as well as in dedicated experiments. Additionally, gyrokinetic simulations are used to test the hypothesis that the impact of magnetic geometry on ion-temperature-gradient-driven turbulence can explain the observations. These simulations are based on specific experimental scenarios and help to identify the geometric features leading to reduced turbulence.

In section 2, the variable magnetic configurations of W7-X, the density fluctuation diagnostic, and the specific plasma scenarios under investigation are described. The experimental results are described in section 3, showing the influence of magnetic configuration on fluctuation data. In section 4, gyrokinetic simulations and an analysis of the underlying mechanisms are presented. Finally, the findings are summarised and discussed in section 5.

2. Experimental setup

2.1. Magnetic configuration space of W7-X

The magnetic field of W7-X is generated by 50 superconducting non-planar modular coils generating the main field and 20 additional superconducting planar coils, which are used to vary the rotational transform by introducing an additional toroidal field component, $\pm B_\phi$. The depth of the toroidal magnetic mirror within each of the 5 field periods of W7-X can be changed by varying the ratio of currents in the non-planar coils [7]. Varying the configuration of W7-X along these two directions, i.e. varying the mirror ratio and the rotational transform, results in a set of paradigmatic configurations. The configuration space of W7-X is far more complex and allows for other variations as well, e.g. in- and outward shifted configurations, low and high magnetic shear configurations. However, in this work, we focus on the following paradigmatic configurations: The *standard* configuration is created by equal currents in the non-planar coil without any additional field by the planar coils. Increasing or decreasing the depth of the magnetic mirrors by adjusting the ratio of currents in the non-planar coils yields the *high* and *low mirror* configuration, respectively. The mirror ratio is used to describe the depth of the magnetic mirror within each field period. It is defined as $(B_0(0) - B_0(\pi/5))/(B_0(0) + B_0(\pi/5))$, where B_0 is the magnitude of the magnetic field on the magnetic axis taken at toroidal angles $\phi = 0$ and $\phi = \pi/5$, i.e. at the corner and centre of the first field period. Figure 1(*b*) shows B_0 for two field periods of the three configurations of W7-X. The low mirror configuration has a mirror ratio of -0.7%, the standard configuration has a mirror ratio of 3.8%, and the high mirror configuration has a mirror ratio of 9.7%. The rotational transform outside the last closed flux surface (LCFS), ι_a, is set to a low rational, which forms island chains in the scrape-off layer (SOL) of W7-X. These are essential for the island divertor installed in W7-X [8]. The standard, high and low mirror configurations have $\iota_a = 5/5$, forming five independent islands. The high iota configuration has an overall higher rotational transform and $\iota_a = 5/4$. The low iota configuration has an overall lower rotational transform and $\iota_a = 5/6$. We neglect configurations with ι_a in between these values, as they can form internal islands and effectively act as limiter configurations due to the missing resonant island chain in the SOL. Figure 1(*a*) shows the radial ι-profiles and the global magnetic shear profiles of low iota, standard, and high iota configuration. While the rotational transform is differs between the configurations from the magnetic axis to the edge, the global magnetic shear is quite similar. In the following, we distinguish two comparison cases with three items each:

(i) low iota—standard—high iota (light to dark red)
(ii) low mirror—standard—high mirror (light to dark blue)

2.2. Core plasma density fluctuation diagnostics

The bulk analysis of this study was performed on line-integrated electron density fluctuation measurements by the Phase Contrast Imaging (PCI) diagnostic of W7-X [9, 12]. For these measurements, an infrared laser beam passes through the entire diameter of the plasma. The (fluctuating) electron density introduces a phase shift to the laser, which leads to scattering on the small-scale spatial structure of turbulent fluctuations. In the optical system after the plasma, the scattered and unscattered components of the beam are separated in the focal plane and phase shifted to each other by a phase plate. This allows for direct interference of the scattered and unscattered components and increased contrast in the image plane at

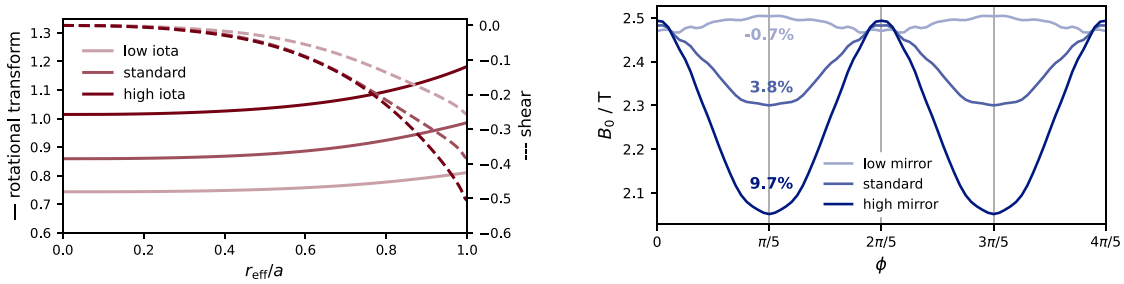

(a) Radial profiles of rotational transform, ι, and global magnetic shear, $\hat{s} = -r\iota'/\iota$ [9].

(b) Magnetic field strength along the magnetic axis illustrating different mirror ratios.

Figure 1. Defining properties of paradigmatic magnetic configurations of W7-X. Panel (*a*) shows the radial ι profile, where r_{eff} is the effective minor radius and a is the value of r_{eff} at the LCFS. Low and high mirror configuration are not depicted since their ι profile is very close to that of the standard configuration. Panel (*b*) shows the magnetic field strength along the magnetic axis, where ϕ is the toroidal angle. Only two field periods of W7-X are shown, since the field is symmetric between field periods. Annotations of the curves represent the mirror ratio. Low and high iota configuration are not depicted since they show similar behaviour as the standard configuration.

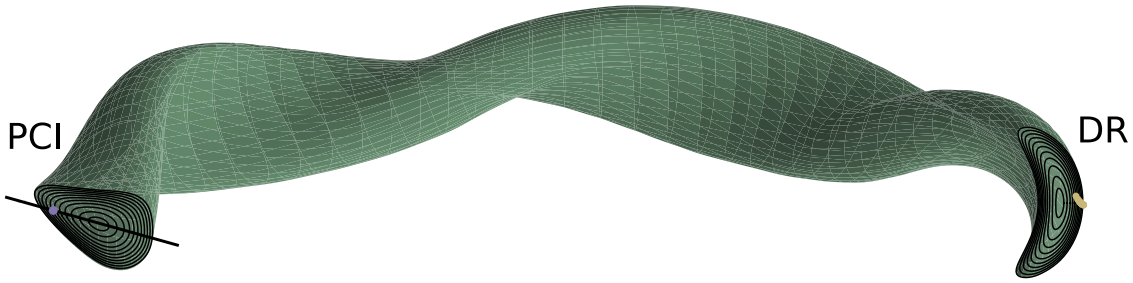

Figure 2. Last closed flux surface of the standard configuration with cross sections at the PCI and DR diagnostic measurement location. Roughly half of the toroidal extent is shown since the diagnostic locations are at almost opposite sides of W7-X. The PCI laser beam passes through the plasma from the inboard to the outboard side [9]. The black solid line illustrates the PCI line of sight, the purple marker lies at the intersection of the $r_{\mathrm{eff}}/a = 0.75$ flux surface. The DR antennas face the outboard midplane of the plasma [10, 11]. The yellow stars mark measurement volumes in an exemplary experiment program.

the detectors. The spatial resolution on the 32-channel array detectors enables the measurement of the binormal wavenumber of fluctuations. Via the poloidal propagation velocities of fluctuations, which is predominantly set by the neoclassical ambipolar radial electric field, in- and outboard side fluctuations can be separated [13]. Figure 2 shows the measurement location in the standard configuration. The cross section in which the PCI diagnostic measures is close to the triangular cross section. The laser beam enters the plasma on the inboard side, passes close to the magnetic axis, and exits the LCFS near the outboard midplane.

A second core density fluctuation diagnostic was used to study differences between magnetic configurations [14]. The Doppler reflectometry (DR) system at W7-X [11, 15] measures radially and wavenumber resolved fluctuations and propagation velocities up to a density-dependent innermost radius. It is located at the outboard midplane of the bean-shaped cross section as seen in figure 2.

2.3. Plasma scenario

In this study, we focus on plasma experiments with electron cyclotron resonance heating (ECRH) and gas fueling from the edge, which is the scenario for long-pulse operation. This type of plasma typically exhibits flat density profiles in the core, peaked electron temperature profiles, and clamped ion temperature profiles [16]. Scenarios that include alternative heating and fueling methods, such as neutral beam injection (NBI) or hydrogen-pellet injection for core fueling, which can lead to improved performance, are not considered here. In the experimental campaign of autumn 2022 to spring 2023, which is referred to as W7-X operation phase 2.1 (OP2.1), dedicated experiments were performed for detailed turbulence measurements and to build a database of fluctuation measurements in various plasma regimes and magnetic configurations. These power step-down programs are described in more detail in appendix A and the corresponding density and temperature profiles at the beginning of section 4. Data from these experiments as well as other experiments of that operation phase fitting the scenario of interest were gathered in a database. The various quantities were down-sampled for the database by averaging over 100 ms segments with stationary plasma behaviour. Transient effects and confinement transitions are therefore not included. Figure 3 shows the range of line-averaged density measured with a single-channel dispersion interferometer [17], $\langle n_e \rangle_l$, and input power, P_{ECRH}, for the two comparison cases of paradigmatic magnetic configurations. Each point represents

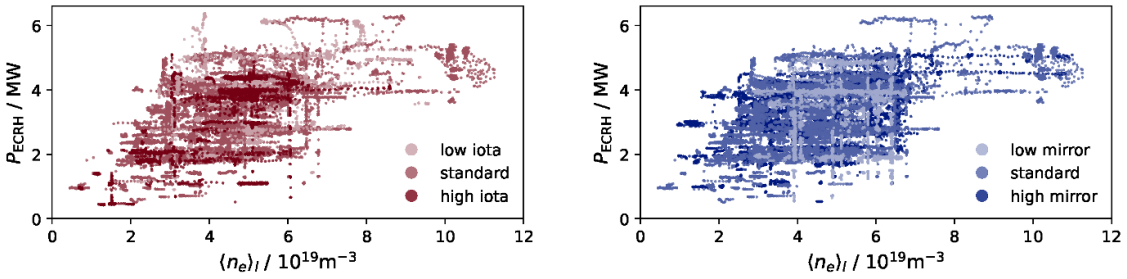

(a) Iota comparison (b) Mirror comparison

Figure 3. Database covering large span of input power and density in the 2022/23 experimental campaign (OP2.1).

the average over a 100 ms stationary segment in a plasma program. Experiments covered a wide range of density and input power and importantly, there are no systematic differences between configurations in the coverage of the parameter range.

3. Experimental results

During the experiments of OP2.1, the PCI diagnostic was continuously measuring and obtained fluctuation data for all operation points shown in figure 3. For an overview of turbulent activity, the absolutely calibrated fluctuation amplitude in the 20 kHz–600 kHz frequency range of the fully line-integrated signal [9] was included in the database. Figure 4 shows the database overview of fluctuation amplitudes over plasma density and heating power. The upper row (figures 4(*a*) and (*b*)) shows the line-averaged fluctuation amplitude measured by PCI for each line-averaged density for the two configuration comparison cases. Instead of displaying the line-integrated values, we chose to normalise to the integration length along the respective line of sight within the LCFS, because this integration length varies between configurations. However, since the PCI diagnostic and the dispersion interferometer share almost identical lines of sight, the difference to displaying line-integrated values is negligible, i.e. the variable integration length within the LCFS for different configurations has no influence on any observed differences in the data. The absolute fluctuation amplitude scales well with the line-averaged density in this plasma scenario [9]. For illustration purposes, a linear regression to the point clouds is shown as a solid line for each configuration. In both comparison cases, a systematic difference in how strongly the fluctuation amplitude scales with the line-averaged density is apparent between the configurations, which is illustrated by the varying slope of the linear regression. There is a clear trend of stronger fluctuations in configurations with lower rotational transform and higher mirror ratio. Note that the ratio of line-averaged density fluctuation amplitude and line-averaged density is not the same as a local fluctuation level, $\tilde{n}_e/\bar{n}_e$, where $\tilde{n}_e$ is the fluctuating electron density and $\bar{n}_e$ is the mean electron density. However, it can be used as a global proxy under the assumptions that the shape of the radial profiles of density and density fluctuation amplitude do not change across the chosen parameter and configuration range (which is discussed later). The fluctuation amplitudes are also known to scale with input power in this scenario, since temperature gradients are increased with increasing input power. The lower row of figures 4(*c*) and (*d*) shows the ratio of line-averaged density fluctuation amplitude and density over ECRH input power. In the same manner as above, linear regression to the points belonging to an individual configuration are shown as solid lines for illustration purposes. The difference in slope in figures 4(*a*) and (*b*) is now represented by a vertical offset. The remaining slope of the fit is due to the scaling with input power, which is weaker than the scaling with density and does not depict a similarly strong dependence on magnetic configuration.

The database overview reveals a robust dependence of turbulent density fluctuation amplitudes on the magnetic configuration for both changes in rotational transform and mirror ratio. An effect in the former comparison case was already observed in a previous study based on data from an earlier experimental campaign [18]. The effect is independent of density or input power levels and affects the line-averaged fluctuation level more than the scaling with input power.

For a more detailed analysis of turbulent fluctuations in different magnetic configurations, we use data from the dedicated experiments with identical plasma parameters (described in more detail in appendix A). The PCI fluctuation amplitude qualitatively shows the same trends between configurations in a direct comparison of similar experiments as observed in the database overview. In total, nine operation points at three different densities and three different ECRH power levels were compared. The observations from all operation points agree qualitatively, which confirms the results of the database approach and stresses the robustness of the experimental result. As a representative example, we focus on an operation point that matches the heating power and density of a previous study in the standard configuration [13]. In the previous study, we found that turbulent fluctuations are predominantly driven by the ion temperature gradient (ITG) mode and are localised in a radial region around $r_{\mathrm{eff}}/a = 0.6 - 0.8$ [13].

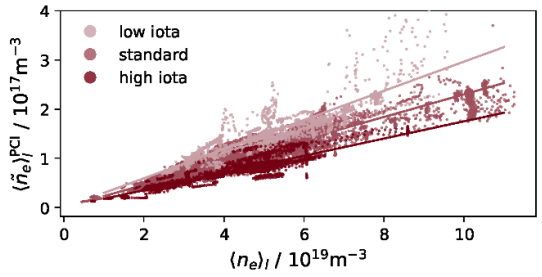

(a) Iota comparison of density scaling.

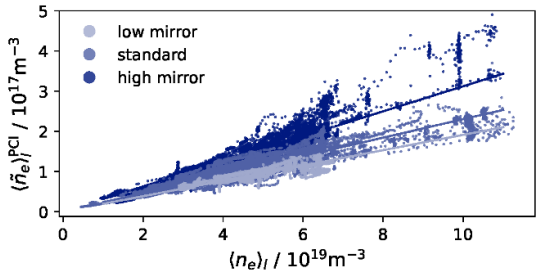

(b) Mirror comparison of density scaling.

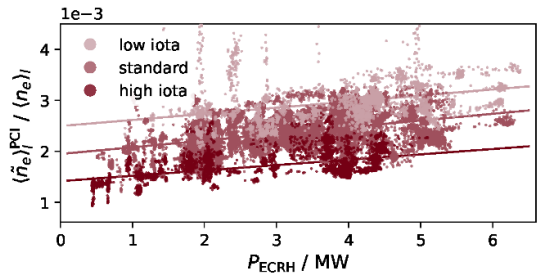

(c) Iota comparison of input power scaling.

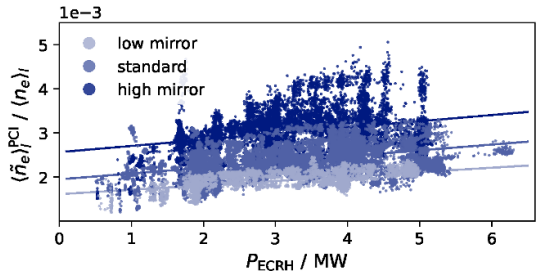

(d) Mirror comparison of input power scaling.

Figure 4. Database approach to fluctuation amplitudes in the 2022/23 experimental campaign (OP2.1).

Density and heating power match well within a configuration comparison but are slightly different between iota and mirror comparison. Thus the standard configuration case is not identical for iota and mirror comparison. Figures 5(*a*) and (*b*) show wavenumber spectra of density fluctuations measured by PCI in the configurations of the iota and mirror comparison case, respectively. For better readability, only the wavenumber spectra from outboard side fluctuations are shown, but both in- and outboard side fluctuation spectra exhibit the same trends. In the cross-section of PCI, the unfavourable curvature is generally larger on the outboard side, leading to larger fluctuation amplitudes [13], which motivates the choice of this branch. Comparing the configurations with different iota, we note that the spectra deviate more strongly in the low wavenumber regime up to 4 cm^{-1}. In the mirror comparison case, the fluctuations differ over the entire measured wavenumber range. The wavenumber spectra have similar shapes, as if scaled by a constant factor.

The data points with the lowest wavenumber show error bars which illustrate the relative uncertainty contribution from the calibration. The difference between the spectra far exceeds the calibration uncertainty and spectral variance, which is strongly reduced by averaging over a long stationary phase (1 s). The experimental wavenumbers cannot be easily translated to normalised binormal wavenumbers, $k_y\rho_i$, since the ion Larmor radius, ρ_i, projection of the binormal wavenumber, k_y, to the PCI measurement direction, as well as $|\nabla \mathbf{y}|$, which sets the contribution of k_y to the perpendicular wavenumber $\mathbf{k}_\perp$, vary along the PCI line of sight [18]. Taking the values at the outboard side at $r_{\mathrm{eff}}/a = 0.75$ as a reference, we note that the presented wavenumber spectra mostly correspond to $k_y\rho_i \lesssim 1$. Typically, ITG modes are destabilised around the ion scale and trapped-electron modes (TEM) at similar or smaller wavelengths. However, in the nonlinear evolution of turbulence, the fluctuation power usually shifts to larger scales, which matches the distribution in the measured wavenumber spectra but does not allow for a direct comparison to the typical scales of the driving instabilities.

The corresponding frequency spectra draw a matching picture, showing larger differences at lower frequencies for the iota comparison and larger differences at higher frequencies for the mirror comparison case.

Measurements by Doppler reflectometers at W7-X support the observations by PCI. In a radial region close to the edge, $0.8 < r_{\mathrm{eff}}/a < 0.9$, for wavelengths in the ion scale, fluctuation levels are observed to be generally larger in the low iota and high mirror configuration than in the standard configuration [14]. This trend agrees with the results from PCI, indicating that the observations are independent of the measurement methods. Furthermore, the agreement between the diagnostics indicates that the trends are not specific to a toroidal region, since the measurement locations of PCI and DR are on opposite sides of W7-X and not directly connected via a field line (see figure 2). Geometry properties such as unfavourable curvature, magnetic field strength, and flux compression within the respective cross sections are quite different, which further supports the interpretation that it is not a geometrical feature which is specific to a certain location that causes the observed differences between magnetic configurations.

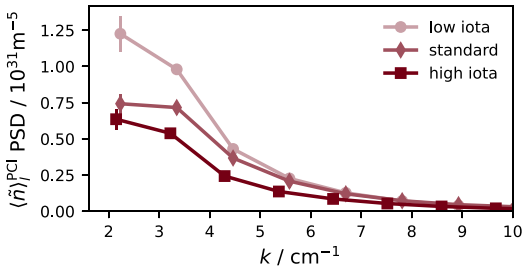

(a) Iota comparison of wavenumber spectra from outboard side fluctuations.

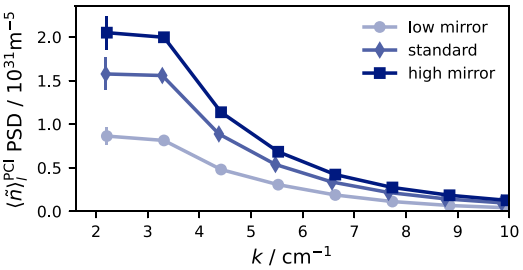

(b) Mirror comparison of wavenumber spectra from outboard side fluctuations.

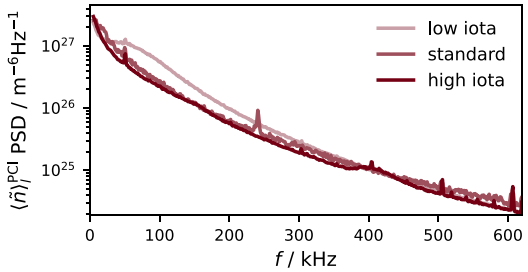

(c) Iota comparison of frequency spectra.

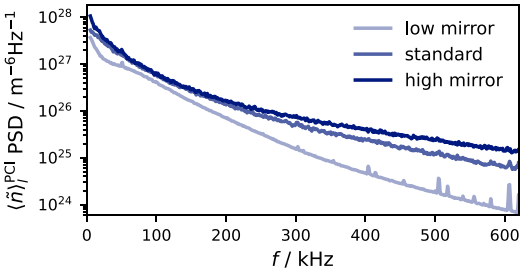

(d) Mirror comparison of frequency spectra.

Figure 5. Wavenumber and frequency spectra at selected operation points. The spectra are depicted as power spectral densities (PSD).

4. Comparison to gyrokinetic theory and modelling

While the fluctuation measurements show clear differences between magnetic configurations in amplitude and spectral distributions, it is not possible to draw definitive conclusions about the underlying mechanisms causing these differences from the fluctuation data alone. The question that arises in this case is whether gyrokinetic theory predicts the observed trends. We distinguish between the drive of turbulent modes, which is contained in the linear physics, and the nonlinear interaction of modes across scales, which leads to saturation. We first focus on differences in the linear destabilisation of modes between the investigated cases and then compare the insights with nonlinear saturated fluctuation levels.

Since the turbulent drive is very sensitive to the radial gradients of density and temperature, we start by discussing the plasma profiles in this scenario. Figure 6 shows the radial profiles of electron density, n_e, electron temperature, T_e, and ion temperature, T_i. Electron density and temperature were measured by the Thomson scattering diagnostic at W7-X [19]. The profiles show the typical features of ECRH plasmas in W7-X: the density is essentially flat in the inner half of the plasma and the electron temperature is very peaked due to ECRH deposition on the magnetic axis. Furthermore, the profile measurements show almost no variation between configurations. Despite the long stationary phase (1 s), which reduces statistical errors, the remaining uncertainties conceal any differences between configurations. This means, given the experimental data with its uncertainty, the potential differences in the electron density and temperature profiles or their gradients between the magnetic configurations cannot be quantified with a reasonable level of confidence.

The ion temperature was provided by charge exchange recombination spectroscopy [20] or by x-ray imaging crystal spectroscopy (XICS) [21, 22]. The former provides more reliable profile measurements but requires active beam emission of NBI blips, which were rarely available in the experiments discussed above. The latter is based on a tomographic inversion which can be prone to systematic errors. Nonetheless, the ion temperature profile shape is very similar between configurations within two thirds of the minor radius. We can apply certain constraints to the T_i profile to ensure it is physically meaningful. In general, $T_i \leqslant T_e$, since ions gain energy only through collisions with electrons in this plasma scenario. The ion temperature stays well below the electron temperature in the plasma core with a moderate gradient up until $r_{\mathrm{eff}}/a \approx 0.6$, where high density and low electron temperature allow for good collisional coupling between electrons and ions, leading to thermal equilibration of the two species, $T_i \approx T_e$, and an increased gradient of T_i. While it is clear that the radial region $r_{\mathrm{eff}}/a \approx 0.7 - 0.8$ exhibits the largest ITG, the uncertainties of the measurement are quite large in this region and some of the inversions from XICS data violate the constraints. It is therefore commonly assumed that $a/L_{T_i} \approx a/L_{T_e}$, where $a/L_X = -a\frac{dlnX}{dr}$ is the normalised inverse gradient length scale, r is the radial coordinate, and X is the respective plasma quantity. Considering these limitations, the potential differences of

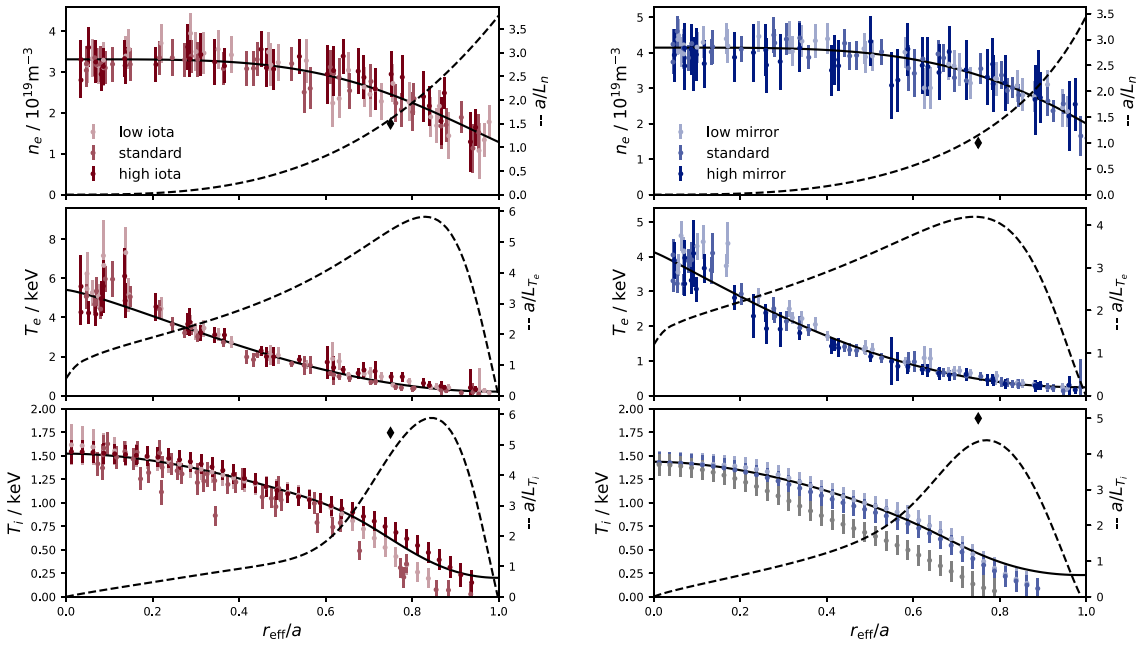

(a) Iota comparison. (b) Mirror comparison.

Figure 6. Plasma profile measurements from dedicated experiments (see appendix A). Model profiles were fitted to represent all three configurations in one comparison case. Normalised inverse gradient length scales are shown on the right vertical axis. Diamonds represent values used for flux tube simulations.

T_i or its gradient between magnetic configurations are smaller than the systematic uncertainties, in particular in the region of largest gradient, despite the fact that the measurement data in figure 6 shows differences. We want to point out that the conclusion is not that there are no differences in the T_i profile but that it is important to be aware of the limitations of the available experimental data and to not assume arbitrary differences.

As mentioned above, the particular operation point was chosen to match a previous study, in which experimental PCI data and gyrokinetic simulations consistently show that the (denormalised) density fluctuation amplitude peaks around $r_{\mathrm{eff}}/a \approx 0.75$ and is generally larger on the outboard side [13]. This is the radial region in which the ITG is particularly large and therefore the drive of ITG modes is the strongest in absolute units. Besides the localisation of fluctuations and the dependence on ITG and density gradient, the structure and frequency of the dominant modes in the simulations of the past study clearly identified them as ITG modes, which is supported by numerous other experimental and numerical findings [18, 23–26]. It is well established that ITG modes are the most relevant driver of turbulent density fluctuations and transport in this operation scenario and in particular at this radial location.

Considering the points of discussion above, we take the following approach to simulations: we focus on the radial region of $r_{\mathrm{eff}}/a \approx 0.75$, since fluctuations are particularly strong there and therefore dominate the signal measured with PCI. Furthermore, we assume the same plasma profiles for each configuration comparison case. For this purpose, model profiles were fitted to the measurement data to represent all three configurations per comparison case. The black solid lines in figure 6 show the model profiles, the dashed black lines show the corresponding gradient length scales. Finally, we will focus on studying ITG modes, which will be further justified by the results of the simulations.

Taking model profiles as the basis for simulations is not just a result of limitations to profile diagnostic data but also fulfils the purpose of isolating the effect of geometry on ITG turbulence. While we try to match the experimental data well with our choice of flux tube and gradients, we do not attempt to validate simulation results to experimental results but try to study possible physical mechanisms leading to the observed trends. This set of assumptions allows us to test the hypothesis that geometry effects on ITG turbulence play a major role in determining density fluctuation levels in W7-X and to identify which aspects of geometry are decisive for the observed differences. If magnetic geometry leads to different turbulence levels and transport, differences in the plasma profiles are to be expected, which in turn alter the turbulence level. Matching the resulting equilibrium turbulence levels and profiles is only possible via self-consistently and simultaneously evolving them by combining global gyrokinetic calculations with neoclassical ones and transport modelling (more to this in section 5). However, these results will hardly be able to provide information on what causes the differences in the first place. We therefore start with a local, linear analysis. In order to be able to estimate the influence of changes in density and ITG, we performed a sensitivity scan in the linear simulations, which will be discussed in section 5.

Table 1. List of the chosen magnetic configurations and magnetic field lines around which simulated flux tubes are centred. The field-line-labelling coordinate α_0 is calculated as $\alpha_0 = \theta_0 - \iota\phi_0$, where ϕ_0 is the toroidal angle at which PCI is located, the rotational transform, ι, is taken at $r_{\text{eff}}/a = 0.75$, and θ_0 is given by the poloidal angle at which the PCI line of sight intersects the $r_{\text{eff}}/a = 0.75$ flux-surface. ϕ_0 is always equal to 4.55, while θ_0 changes with the geometry. The second column lists the W7-X Team-internal identifier for equilibrium runs of the Variational Moments Equilibrium Code (VMEC) [27, 28], which provide the magnetic equilibrium for the given coil currents and experimental plasma pressure of each configuration.

Configuration	VMEC run ID	θ_0	ι	α_0
low iota	019	0.23	0.77	−3.278
standard	352	0.13	0.91	−4.025
high iota	311	0.17	1.08	−4.746
low mirror	022	0.14	0.90	−3.961
standard	169	0.15	0.90	−3.975
high mirror	339	0.16	0.91	−3.982

4.1. Linear flux tube gyrokinetic simulations with `stella`

Linear flux tube simulations are performed using the δf-gyrokinetic code `stella` [29], which has been previously successfully applied to study electrostatic turbulence in comparison to experimental fluctuation data from Doppler reflectometry [25]. The effects of kinetic electrons are retained, and the magnetic configuration is varied in order to study its effect on electrostatic microinstabilities. The magnetic equilibria are based on the experimental scenario and represent runs of the VMEC [27, 28] with the corresponding coil currents and central plasma pressure from the experiment. In total, six different magnetic equilibria are selected. For each configuration, simulations are performed in the flux tube that crosses the PCI line of sight on the outboard side at a normalised radius of $r_{\text{eff}}/a = 0.75$. The simulations should thus capture the fluctuations that have the largest impact on the PCI measurement signal despite being radially local. Details about the configurations and the simulated magnetic field lines are reported in table 1.

Electrostatic, collisionless plasmas are simulated. As discussed above, density and ITGs from model profiles in figure 6 and are kept constant throughout a single geometry scan. For the iota scan, $\{a/L_{Ti}, a/L_n\} = \{5.4, 1.5\}$, while for the mirror scan, $\{a/L_{Ti}, a/L_n\} = \{5.0, 1.0\}$. The ion-to-electron temperature ratio, $\tau = T_i/T_e$, can be set to a good approximation to one. Following the choice of focusing on ITG modes, the electron temperature gradient a/L_{Te} is set to zero in order to isolate the impact of the geometry on the ion temperature and density gradient drive. This choice is further justified by results presented in appendix B, where results obtained for $a/L_{Te} = a/L_{Ti}$ show that the presence of electron temperature gradients do not qualitatively change the turbulence drive, which remains of the ITG type, and thus the effect of the geometry on it.

The phase-space coordinates used by `stella` are $(x, y, z, v_\parallel, \mu)$. The real space is parametrized by field-aligned coordinates. Specifically, the magnetic field is written in Clebsch coordinates, $\mathbf{B} = (\mathrm{d}\psi_t/\mathrm{d}r_{\text{eff}})\boldsymbol{\nabla}\mathbf{r}_{\text{eff}} \times \boldsymbol{\nabla}\boldsymbol{\alpha}$ [30], where $r_{\text{eff}} = a\sqrt{\psi_t/\psi_{t,\text{LCFS}}}$ is the effective minor radius, ψ_t is the toroidal flux divided by 2π and $\psi_{t,\text{LCFS}}$ its value at the LCFS. The field-line-labelling coordinate is $\alpha = \theta - \iota\phi$, where ϕ and θ are straight-field line coordinates, with ϕ the toroidal angle and θ the poloidal PEST coordinate [31]. The cross section perpendicular to the magnetic field is defined by $x = r_{\text{eff}} - r_{\text{eff},0}$ and $y = r_{\text{eff},0}(\alpha - \alpha_0)$, with $r_{\text{eff},0}$ and α_0 denoting the magnetic field line at the centre of the flux tube. From this follows that the evolved gyrokinetic equation [32] can be Fourier transformed in the plane perpendicular to the magnetic field and the perpendicular wavevector decomposed as $\mathbf{k}_\perp = k_y\boldsymbol{\nabla}\mathbf{y} + k_x\boldsymbol{\nabla}\mathbf{x}$. The parallel coordinate is taken here to be the toroidal angle, $z = \phi$. The velocity space is parametrised by the parallel velocity, $v_\parallel$, and the magnetic moment, $\mu = v_\perp^2/2B$. The simulated flux tubes are all centred at the PCI location, $\phi_0 = 4.55$, and the following resolutions are used: $(n_\phi \times n_{v_\parallel} \times n_\mu) = (128 \times 64 \times 24)$. For each configuration, one poloidal turn is simulated.

The chosen flux tubes have a geometry that is more *exotic* than the largely explored flux tube centred at the outboard midplane of the bean-shaped cross section, where the region of worst curvature is located and thus where ITG turbulence is expected to peak [33]. At this location, the flux tube cross section is perpendicular and the fastest growing modes are characterised by $k_x = 0$, which minimises FLR effects (i.e. minimises the perpendicular wavevector magnitude $k_\perp = \sqrt{k_x^2|\boldsymbol{\nabla}\mathbf{x}|^2 + k_y^2|\boldsymbol{\nabla}\mathbf{y}|^2 + 2k_xk_y\boldsymbol{\nabla}\mathbf{x}\cdot\boldsymbol{\nabla}\mathbf{y}}$ if $\boldsymbol{\nabla}\mathbf{x}\cdot\boldsymbol{\nabla}\mathbf{y} = 0$). In this work, however, the choice of flux tube is adapted to the PCI location. If the flux tube is centred where the PCI line of sight intersects the chosen flux surface, the flux tube cross section is neither perpendicular at the region of worst curvature, nor at the one where finite Larmor radius effects are minimised. Consequently, we cannot assume the fastest growing modes in these flux tubes to be characterised by $k_x = 0$ and thus choose to simulate a range of finite radial wavenumbers, both positive and negative. This takes into account the possibility of $k_\perp$ to be minimised at locations along the flux tube where the cross section is not perpendicular and thus where modes have twisted wavefronts. The choice of simulating both positive and negative k_x is motivated by the fact that such flux tubes are not stellarator symmetric.

For the above-mentioned reasons, a comprehensive scan of growth rate spectra at ion scales, i.e. modes characterised by $k_\perp\rho_i \approx 1$, is performed first. The choice of the binormal and radial wavenumber ranges follows the expectation that the analysed plasmas are dominated by ITG turbulence. The binormal wavenumber is varied in the range $k_y\rho_i \in [0.4, 1.6]$ and the radial wavenumber in the range $k_x\rho_i \in [-5, 5]$. As observed in [34], $k_y\rho_i < 2$ and $k_x\rho_i < 2$ are enough to capture the fastest growing mode for moderate density gradients.

The result for the growth rate spectra is shown in figure 7, while in table 2, the fastest growing modes and the respective growth rates are reported. All spectra are characterised by two distinct branches, one around $k_x\rho_i = 0$ and the other

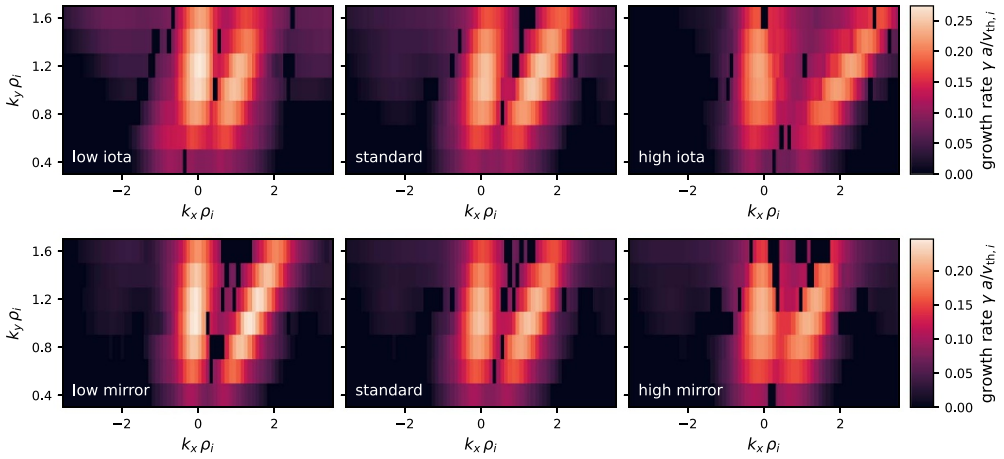

Figure 7. Scan of linear simulations with `stella` for $k_y\rho_i$ and $k_x\rho_i$ in the ion scale range. Depicted is the normalised growth rate as a heat map for the configurations in the iota (upper row) and mirror (lower row) comparison case.

Table 2. Fastest growing mode in each configuration. The binormal $k_y\rho_i$ and radial $k_x\rho_i$ wavenumbers at which it is destabilised and the respective growth rate $\gamma a/v_{th,i}$ are reported.

Configuration	$k_y\rho_i$	$k_x\rho_i$	$\gamma a/v_{th,i}$
low iota	1.2	0.05	0.27
standard	1.1	1.46	0.25
high iota	1.1	−0.15	0.23
low mirror	1.1	−0.05	0.25
standard	1.0	−0.05	0.22
high mirror	1.1	−0.05	0.21

with finite $k_x\rho_i$. The two branches are more or less destabilised depending on the configuration. We observe a decrease of about 10% in the magnitude of the growth rate when moving from a lower to a higher iota configuration. Moreover, the position in (k_x, k_y) space of the right branch is shifted to the right with increasing iota. As a consequence, the position of the fastest growing mode also shifts with increasing iota, as also visible from table 2. For the mirror scan, this does not occur, but the overall stability of the two branches increases with increasing mirror ratio. In particular, we again observe a decrease of around 10% in the magnitude of the growth rate with increasing mirror ratio. We can compare the simulated growth rates to the experimental observations. Since nonlinear interaction of modes and saturation, which ultimately determine the experimentally measurable fluctuations, are not included in the linear simulations, it is only valid to check if the trends with magnetic configurations qualitatively agree. However, experience from past studies shows that studying the growth rates usually gives a good indication of the final fluctuations. In the case of the iota scan, the trend in simulated growth rates matches the experimentally observed trend. In contrast, in the mirror scan, the trends do not match. This indicates that in the iota scan, the magnetic geometry effect on the linear ITG drive of turbulence is indeed the mechanism causing the experimentally observed trend, while in the mirror scan, other effects have to play a larger role.

A further scan in the normalised binormal wavenumber $k_y\rho_i \in [0.1, 10]$ is performed while keeping the normalised radial wavenumber $k_x\rho_i = 0$. This is a valid approximation, given the result of the complete growth rate spectra reported in figure 7. The extension of the binormal wavenumber range is helpful for the characterisation of instabilities with shorter wavelengths. The results are reported in figures 8(*a*) and (*b*), where, however, only a limited, more relevant range of binormal wavenumbers is shown.

The growth rate spectra of both the iota and mirror scan are dominated by an ITG mode at $k_y\rho_i \approx 1$. At smaller scales, $k_y\rho_i > 3$, short-wavelength ITG modes (SWITG) are observed [35–38]. These modes show a similar eigenmode structure as the larger scale ITG. Since such small scales are much less relevant for the nonlinear fluctuation spectra and for transport, we will not analyse these modes in detail. The spectra comparison for the iota scan reveals a similar trend and growth rate difference to that observed for the most unstable mode in (k_x, k_y) space. The main ITG peak around $k_y\rho_i \approx 1$ exhibits a configuration-dependent difference of approximately 10% when iota decreases. However, at higher wavenumbers, the trend becomes less distinct. In the spectra comparison for the mirror ratio scan, the trend at $k_y\rho_i \approx 1$ is less distinct, particularly when transitioning from the high mirror to the standard configuration, which feature nearly identical growth rates. The difference becomes more pronounced at higher wavenumbers, suggesting that trapped electrons play a more significant role in destabilisation (or stabilisation).

In the discussion so far, the electron temperature drive has been excluded to isolate the physics of the dominant ITG mode. In appendix B, growth rate spectra for a scan in $k_y\rho_i$ analogous to figure 8 are shown, for which an equal ion and electron temperature gradient, $a/L_{T_e} = a/L_{T_i}$, was assumed. Including the electron temperature drive overall increases the growth rates but changes neither the structure of the dominant modes nor the trends observed by varying the magnetic configuration. We conclude that the effect of electron temperature drive is not relevant for difference between magnetic configurations, which justifies the assumption that the ITG drive is

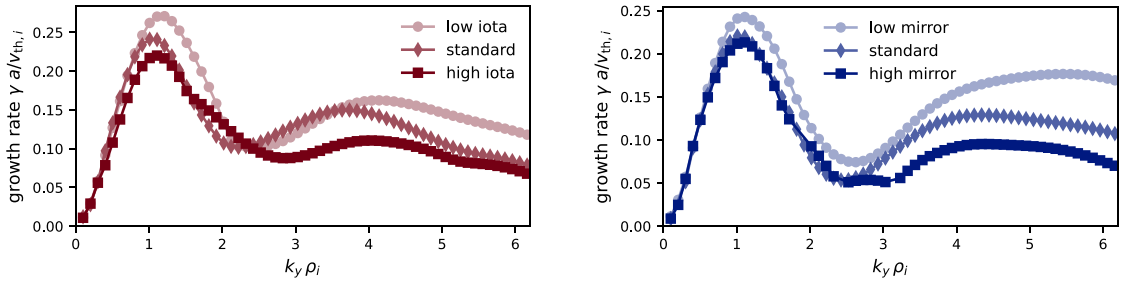

(a) Iota comparison of growth rate spectra, $\{a/L_{Ti}, a/L_n\} = \{5.4, 1.5\}$.

(b) Mirror comparison of growth rate spectra, $\{a/L_{Ti}, a/L_n\} = \{5.0, 1.0\}$.

Figure 8. Growth rate spectra from linear gyrokinetic simulations with $a/L_{T_e} = 0$ for a scan of $k_y\rho_i$ at $k_x\rho_i = 0$.

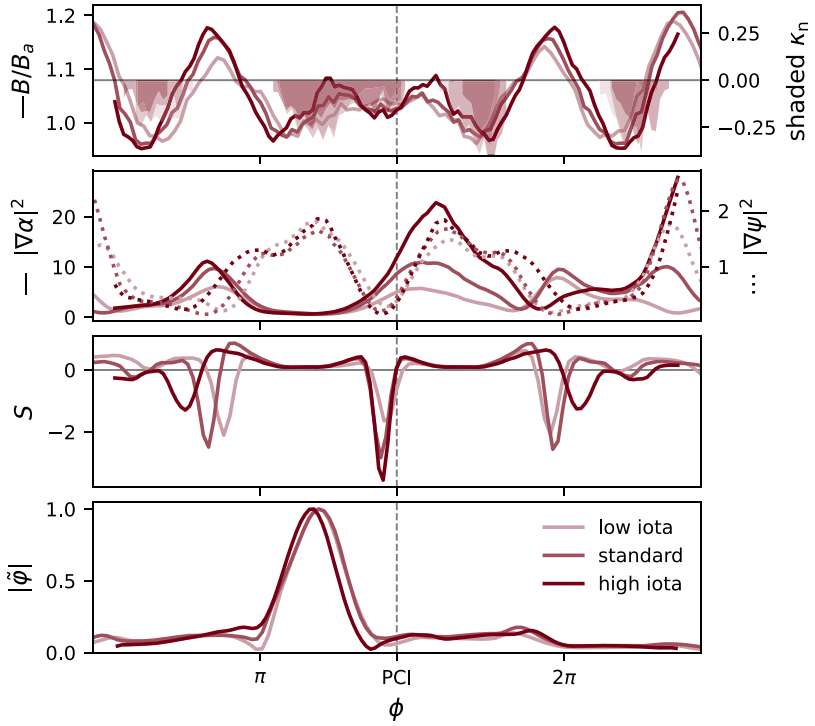

Figure 9. The upper three panels show geometric quantities relevant for turbulent micro-instabilities along the $r_{\mathrm{eff}}/a = 0.75$ flux tube crossing the PCI line of sight. These are the magnitude of the magnetic field, B/B_a; the curvature drift in the binormal direction, κ_n; the metric coefficients $|\boldsymbol{\nabla\alpha}|^2$ and $|\nabla\psi|^2$; and the local magnetic shear, S. The lower panel shows the fastest growing mode eigenfunctions for the iota scan simulations with $k_x\rho_i = 0$. Here, $|\tilde{\varphi}|$ is the potential fluctuation magnitude normalised to its maximum value.

the relevant mechanism, in retrospect. Therefore, we continue by studying geometry quantities in the various magnetic configurations in comparison to the dominant ITG mode.

4.2. Effect of magnetic geometry on dominant ITG modes

In order to understand the growth rate dependence on geometry, the eigenfunctions of the fastest growing mode for the spectra in figures 8(*a*) and (*b*) are compared to relevant geometric quantities along the magnetic field lines. The results are presented in figures 9 and 10. For every case in both scans, the electrostatic potential structure, $|\tilde{\varphi}| = (a/\rho_i)(e/T_i)|\varphi|$, of the fastest growing mode peaks at the closest magnetic drift well—denoted by negative values of the binormal curvature drift, $\kappa_n = B_a a/B^2\,(\mathbf{B}\times\boldsymbol{\kappa}\cdot\boldsymbol{\nabla\alpha})$ with $B_a = 2|\psi_{t,\mathrm{LCFS}}|/a^2$, which is proportional to the normal curvature and marked as a shaded region in the first panel of figure 9. This drift well is found roughly at the location of the bean-shaped cross section at $\phi = 1.2\pi$. We note that the second branch present in figure 7 corresponds to eigenfunctions peaking at the other closest magnetic drift well, to the right of the PCI location. The PCI location is in fact between two drift wells corresponding to the two closest bean-shaped cross sections.

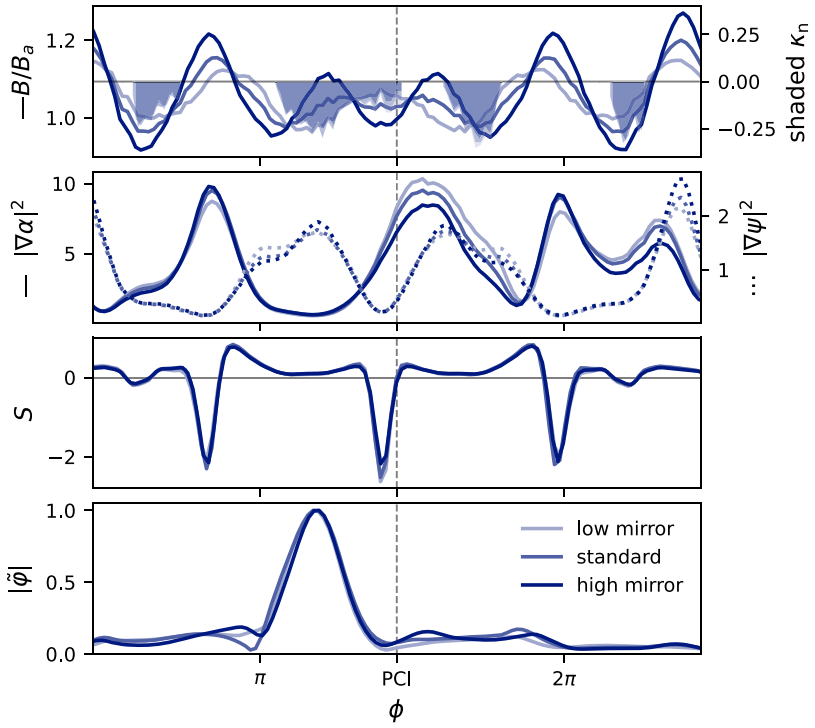

Figure 10. The upper three panels show geometric quantities relevant for turbulent micro-instabilities along the $r_{\text{eff}}/a = 0.75$ flux tube crossing the PCI line of sight. The quantities are the same as for the iota scan in figure 9. The lower panel shows the fastest growing mode eigenfunctions for the mirror scan simulations with $k_x\rho_i = 0$.

For both scans, some of the geometric quantities differ only marginally between the configurations. For the iota scan, the only quantity that shows a significant difference is $|\nabla\boldsymbol{\alpha}|^2$, representing the density of field lines in the binormal direction. The flux compression, $|\nabla\psi|^2$, which is often associated with a large effect on the destabilisation of ITG modes [4, 39], does not seem to be relevant for the observed differences. For configurations with higher ι, $|\nabla\boldsymbol{\alpha}|^2$ is increased along the field line. There are two effects associated with this: high values of $|\nabla\boldsymbol{\alpha}|^2$ increase the perpendicular wavenumber, $k_\perp$, and lead to stronger FLR suppression of modes. Additionally, the strong increase of $|\nabla\boldsymbol{\alpha}|^2$ along the flux tube is connected to a peak of local magnetic shear, $S = a\mathbf{B}\cdot\nabla\left(\frac{\nabla\psi\cdot\nabla\boldsymbol{\alpha}}{|\nabla\psi|^2}\right)$ [40], which is shown in the third panel of figure 9. The local magnetic shear measures the parallel variation of the angle between $|\nabla\boldsymbol{\alpha}|^2$ and $|\nabla\psi|^2$ and its strong increase in the high iota configuration is connected to the much stronger plasma shaping.

Both effects lead to localisation and stabilisation of eigenfunctions [39, 41–43]. This can be seen clearly in shape of the eigenfunction of the fastest growing modes in the last panel of figure 9. As mentioned above, the modes peak in the closest drift well. We find the fastest growing mode in this drift well, since this region is also characterised by very low values of $|\nabla\boldsymbol{\alpha}|^2$ and $|S|$, it is not surprising that these are the fastest growing modes in the flux tube. The strong increase of $|\nabla\boldsymbol{\alpha}|^2$ to either side along the flux tube and the corresponding peak of local magnetic shear strictly limit the toroidal extent of the mode, i.e. it is boxed in [42]. This effect also decreases the overall growth of the dominant mode and is stronger for configurations with higher iota. The trend is consistent with the lower growth rates observed in linear simulations and with the lower fluctuation amplitudes observed in experiments. We expect the effect of $|\nabla\boldsymbol{\alpha}|^2$ and local shear to play a role for modes that are located in other drift wells (e.g. the aforementioned finite-$k_x\rho_i$ modes) and their nonlinear interaction. Following this argument, we expect the trend to translate well or even be increased in nonlinear fluctuation amplitudes. The effect of $|\nabla\boldsymbol{\alpha}|^2$ and local shear can also be observed in the flux tube centred at the bean-shaped cross section, which matches the experimental agreement between PCI and DR measurements. Finally, the increase in iota decreases the extent of the drift wells. This can also play a role in the stabilisation of the fastest growing modes.

The geometry of the configurations selected for the mirror scan exhibits even less variation. From the comparison with the geometry, it is evident that changing the mirror ratio has very little effect on the local shear, metric coefficients and binormal curvature drift. The crucial difference between the configurations lies in the depth and location of magnetic field wells. A lower mirror ratio results in a lower fraction of trapped particles. Trapped electrons are known to drive TEMs and contribute to ITG and mixed/hybrid modes [44, 45]. As noted in [46], while trapped particles do not drive ITG modes, they can exacerbate them by altering their *inertia*. The destabilisation is proportional to the fraction of trapped particles seen by the potential. However, the influence

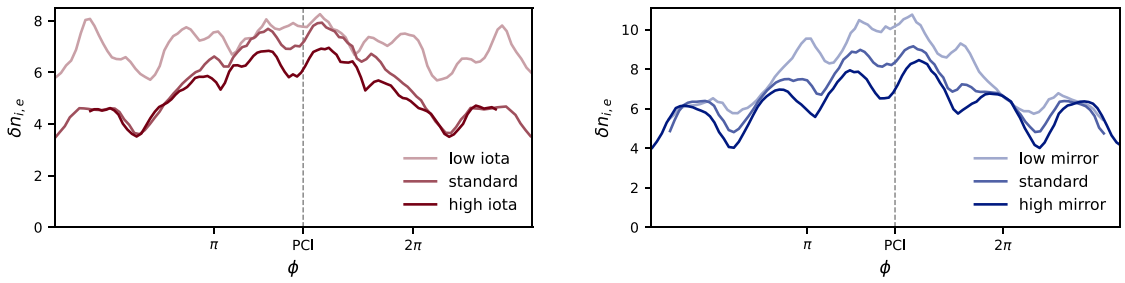

(a) Iota scan comparison. (b) Mirror scan comparison.

Figure 11. Nonlinear saturated density fluctuation amplitude along the simulated $r_{\text{eff}}/a = 0.75$ flux tube crossing the PCI line of sight.

of trapped electrons also depends on the overlap of magnetic field wells and unfavourable curvature [47–49]. This is described by the maximum-J property of the configurations, where J is the second adiabatic invariant. In maximum-J geometries, deeply trapped particles are displaced from regions of unfavourable curvature [49]. As previously noted in [50], the high mirror configuration exhibits a stronger maximum-J property than the standard configuration, which in turn is stronger than the low mirror configuration in this property. Consequently, although a higher mirror ratio is associated with a larger fraction of trapped particles, this does not necessarily lead to greater instability. On the contrary, in configurations with maximum-J property, trapped electrons even have a stabilising influence on ITG [45]. In the present analysis, this is evident in the top panel of figure 10. In the closest drift well, where the electrostatic potential of the fastest growing modes peak, the high mirror configuration features a magnetic field hill, while the low mirror configuration exhibits a magnetic field well, with the standard configuration falling between the two. This observation aligns with the lower growth rates predicted by linear simulations as the mirror ratio increases but does not match the experimental observation which features larger density fluctuations as the mirror ratio increases. As observed in figure 8(b), the effect of the mirror ratio, and thus of the maximum-J property, on growth rates is even more evident at shorter wavelengths ($k_y\rho_i > 3$). This is likely an effect of the stronger localisation of SWITG modes [38], which exacerbates the difference of how many trapped particles are seen by the potential when varying the mirror ratio.

4.3. Nonlinear flux tube gyrokinetic simulations with `stella`

So far, we used linear simulations to investigate the effect of geometry on the driving instabilities of turbulence and the relevant mechanisms for difference between the configurations. However, experimental time scales are longer and the fluctuation amplitudes are too large for the linear description to hold in a direct comparison to experimental quantities. For this reason, in order to directly compare gyrokinetic predictions with measured density fluctuations and to study whether the trends observed in the linear drive of turbulence translate into the saturated phase of turbulence, nonlinear simulations are required. At first, flux tube simulations are considered and the gyrokinetic code `stella` is employed. A similar resolution along the field line as in linear simulations is used but with reduced resolution in velocity space to lower computational cost: $(n_{v_\parallel} \times n_\mu) = (36 \times 24)$. The minimum simulated binormal wavenumber is $(k_y\rho_i)_{\text{min}} = 0.05$, while the maximum is $(k_y\rho_i)_{\text{max}} \approx 2.5$. The minimum and maximum simulated radial wavenumbers vary depending on the chosen configuration due to constraints imposed by the twist-and-shift boundary conditions. On average, these values are approximately $(k_x\rho_i)_{\text{min}} \approx 0.05$, and $(k_x\rho_i)_{\text{max}} \approx 3.3$.

Table 3. Value of the density fluctuations amplitude at the toroidal angle $\phi_0 = 4.55$, where the PCI line of sight crosses the simulated flux tubes.

Configuration	$\delta n_{i,e}$
low iota	7.78
standard	7.18
high iota	6.13
low mirror	10.18
standard	8.35
high mirror	6.13

The same assumptions made for linear simulations are applied to the nonlinear simulations as well. Namely, electromagnetic effects and collisions are neglected. Plasma parameters are taken from the same plasma profiles used for linear simulations and are kept fixed for each configuration scan, to also isolate the effects of geometry on saturation mechanisms. Detailed information on the gradients were reported in the previous subsection.

To compare with experimental data, we extract information about density fluctuations. Specifically, we analyse their amplitude, and perform a time average over the saturated nonlinear phase $\delta n(\phi) = \left\langle \sum_{\mathbf{k}} \sqrt{|\delta n_{\mathbf{k}}|^2} \right\rangle_t (\phi)$. Figure 11 shows the structure of density fluctuations along the magnetic field line for both configuration scans. The stabilisation trends observed in linear simulations persist in the nonlinear regime: increasing iota or the mirror ratio reduces density fluctuations. Table 3 presents the density fluctuation values extracted at $\phi_0 = 4.55$,

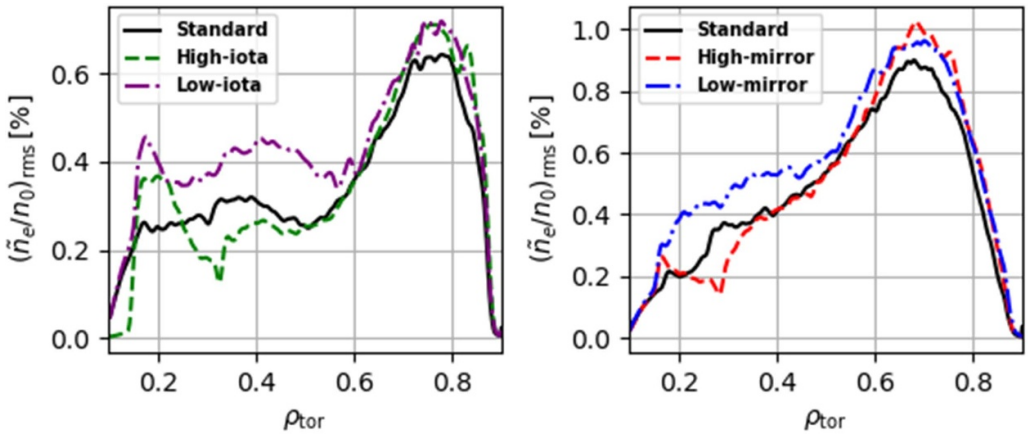

Figure 12. Radial profiles of nonlinear saturated density fluctuation level (RMS of $\tilde{n}_e/n_0$ in percent) from global simulations with GENE-3D for the iota scan comparison (left panel) and the mirror scan comparison (right panel).

where the PCI line of sight intersects the simulated flux tubes. These values indicate a reduction in density fluctuations of approximately 10% when iota is increased and around 20% when the mirror ratio is increased. While the former trend aligns with experimental observations, the latter is consistent with linear predictions but contradicts experimental results.

4.4. Nonlinear global gyrokinetic simulations with GENE-3D

Finally, to investigate whether the discrepancy in the observed trend is due to limitations of the local flux tube gyrokinetic model, we also present global gyrokinetic results. These simulations were performed using the GENE-3D code [51, 52], which incorporates gyrokinetic ions and electrons with a realistic ion-to-electron mass ratio, electromagnetic effects, and a background radial electric field. The same equilibrium magnetic field is used as for the `stella` flux tube simulations, and selected magnetic quantities are mapped for use in GENE-3D through the intermediate interface GVEC [51]. The simulations cover the radial domain $\rho_{\mathrm{tor}} = [0.1, 0.9]$, where $\rho_{\mathrm{tor}} = \sqrt{\psi_t/\psi_{t,\mathrm{LCFS}}}$. The spatial grid resolution is $(n_x \times n_y \times n_z) = (300 \times 256 \times 64)$ in the radial (x), bi-normal (y), and field-aligned (z) directions, and the velocity grid resolution is $(n_{v_\parallel} \times n_\mu) = (64 \times 16)$ for the velocity parallel to the magnetic field $v_\parallel$ and the magnetic moment μ. The simulations are performed in gradient-driven mode, with Krook-type operators applied to particles and heat in order to preserve the plasma plasma profiles shown in figure 6. Additionally, buffer regions covering 5% of the radial domain are implemented near the boundaries to satisfy Dirichlet boundary conditions. These regions include a Krook damping operator to suppress fluctuations.

In figure 12, we present the radial profiles of nonlinear saturated density fluctuation amplitudes (in arbitrary units, A.U.) from global simulations using GENE-3D for two scans: the iota scan (left panel) and the mirror scan (right panel). The global GENE-3D results align with the flux tube simulations, though the effects are less pronounced. In the iota scan, fluctuations are higher for the low iota configuration and lower for the high iota configuration. Similarly, in the mirror scan, fluctuations are elevated for the low mirror configuration and reduced for the high mirror configuration.

At this stage, both experimental data and gyrokinetic simulations provide clear results, but we find good agreement of trends in the iota comparison case and a disagreement between experimental and gyrokinetic results in the mirror comparison case. The discrepancy in the latter case does not seem to be caused by local or global effects, since the respective simulations show agreement. The trend observed in flux tube simulations is reduced in the global simulations but not reversed. The impact of geometry on the growth of dominant modes and on the nonlinear development of turbulence at fixed plasma profiles is apparently not the relevant mechanism for causing differences in turbulence levels in the mirror scan. Although not shown here, neither the local nor the global simulations match the experimental power balance. To resolve this issue, it is necessary to evolve the profiles self-consistently with the experimental sources, as discussed at the beginning of section 4. This approach has been demonstrated recently in Fernando *et al* 2025 [26] using the GENE-KNOSOS-TANGO framework [53] across four different scenarios of the 2018 W7-X experimental campaign. In that study, the simulated density and temperature profiles showed good agreement with experimental data, and the density fluctuations and turbulent heat diffusivities were well-aligned with the experimental observations. By adopting this method, we could obtain profiles that are compatible with the experimental data while simultaneously achieving agreement with the experimental power balance. With this approach, differences in the plasma profiles and their gradients can be assessed and related to the equilibrium turbulence levels.

5. Summary and discussion

We identify the need to experimentally study magnetic configuration effects on turbulence in optimized stellarators to support stellarator optimisation for reduced turbulent transport. This is now possible as experimental fluctuation data

from W7-X becomes available for a larger parameter and configuration space and numerical tools for turbulence simulations become more powerful and feasible. Two ways to vary the magnetic configuration in W7-X are explored, low to high iota and low to high mirror configurations. Density fluctuation data measured by the PCI diagnostic shows robust trends for both cases. We observe general trends in a database approach as well as matching differences in a direct comparison at nine different operation points. The observations match results from previous experiments and other fluctuation diagnostics.

Measured density fluctuation amplitudes are lower in the high iota configuration. The difference appears predominantly at lower wavenumbers. Gyrokinetic flux tube simulations with `stella` reproduce the trend in ITG growth rate spectra and nonlinear density fluctuation amplitudes. Global gyrokinetic simulations with GENE-3D largely support this picture. In these simulations, the same density and temperature gradients were assumed for all configurations. By isolating the effect of magnetic geometry, we can confirm the hypothesis that its impact on ITG modes, the dominant driving mechanism for turbulence, is likely the source of the experimentally observed trend. An analysis of the relevant geometric quantities reveals a strong connection to the $|\nabla\boldsymbol{\alpha}|^2$ metric, which measures the density of field lines and is connected to local magnetic shear and FLR effects limiting the toroidal extent of ITG modes. For the first time, we can experimentally show the effect of a specific geometry property of an optimised stellarator configuration on ITG turbulence. The effect is related to mechanisms also used in critical-gradient optimisation for reducing turbulence in stellarators [4, 39]. However, it is unclear whether the reduction in fluctuation amplitude results in an improved confinement or higher temperatures. As mentioned above, a self-consistent evolution of turbulence and plasma profiles is required to complete the picture. We performed a sensitivity scan of the linear growth rates to estimate the effect of potentially resulting differences in density and ITG length scales. A $\pm 20\%$ variation of a/L_{T_i} causes almost $\pm 20\%$ variation of the growth rates and thus exceeds the differences due to magnetic geometry. A $\pm 20\%$ variation of a/L_n only causes a variation of the growth rates that is much smaller than the differences due to magnetic geometry. Furthermore, a more in-depth analysis of the impact of geometry on nonlinear effects will be subject of an upcoming second publication. In particular, the impact of magnetic geometry on the growth and interaction of secondary modes and the configuration dependent shift of nonlinear wavenumber spectra are of interest.

In the comparison of low mirror, standard and high mirror configuration, experimental density fluctuation measurements show lower amplitudes in the former case. The entire resolved wavenumber range is affected to the same extent, i.e. the difference is not exclusive to a specific wavenumber regime. Gyrokinetic theory predicts a reduction of destabilisation and even stabilisation by trapped electrons when approaching maximum-J configurations, which is the case going from the low to the high mirror configuration. Flux tube simulations with `stella` confirm this prediction with larger growth rates and density fluctuation amplitudes in the low mirror case. Global GENE-3D simulations show a reduced but not a reversed trend compared to the flux tube simulations. While experimental measurements and gyrokinetic simulations show clear results, they disagree on the direction of the trend. It seems clear that the discrepancy is neither caused by a global/-local effect, nor a linear/nonlinear effect, since the simulations agree in all settings and measurements by diagnostics in different locations show consistent results. The details of the nonlinear behaviour in these configurations will be discussed in the aforementioned upcoming publication. Furthermore, including the electron temperature gradient in simulations, which was neglected for the flux tube simulations, does not reverse the trend as seen in the linear growth rates in appendix B and global GENE-3D simulations. However, we do note that including impurities, which were not considered in this study, can have an impact not only on ITG but in connection to electron temperature gradient driven modes as well [54]. The largest remaining unknown are the detailed gradients of density, ion and electron temperature. As discussed for the iota case, the self-consistent evolution of turbulence and plasma profiles is required to complete the picture and is planned for an upcoming publication. The same sensitivity scan of growth rates was performed as for the iota scan with identical results. This means, variations of a/L_{T_i} on the order of $\pm 20\%$ are sufficient but also required to reverse the trend between configurations.

Acknowledgments

The authors would like to thank P Costello and E Rodríguez for the fruitful discussions. This work has been carried out within the framework of the EUROfusion Consortium, funded by the European Union via the Euratom Research and Training Programme (Grant Agreement No. 101052200–EUROfusion). Views and opinions expressed are however those of the author(s) only and do not necessarily reflect those of the European Union or the European Commission. Neither the European Union nor the European Commission can be held responsible for them. Support for the MIT and SUNY-Cortland participation was provided by the US Department of Energy under Grant Number DE-SC0014229.

Appendix A. Power step down experiments

The power step programmes were designed to cover a large range of density and input power in various configurations in a reproducible way. Figure A1 shows an overview of these dedicated turbulence study programmes. The ECRH input power starts at the highest available power and was reduced in steps at a feedback-controlled constant line-integrated density. The ECRH power was modulated for 0.5 s in each step to enable heat pulse propagation measurements with

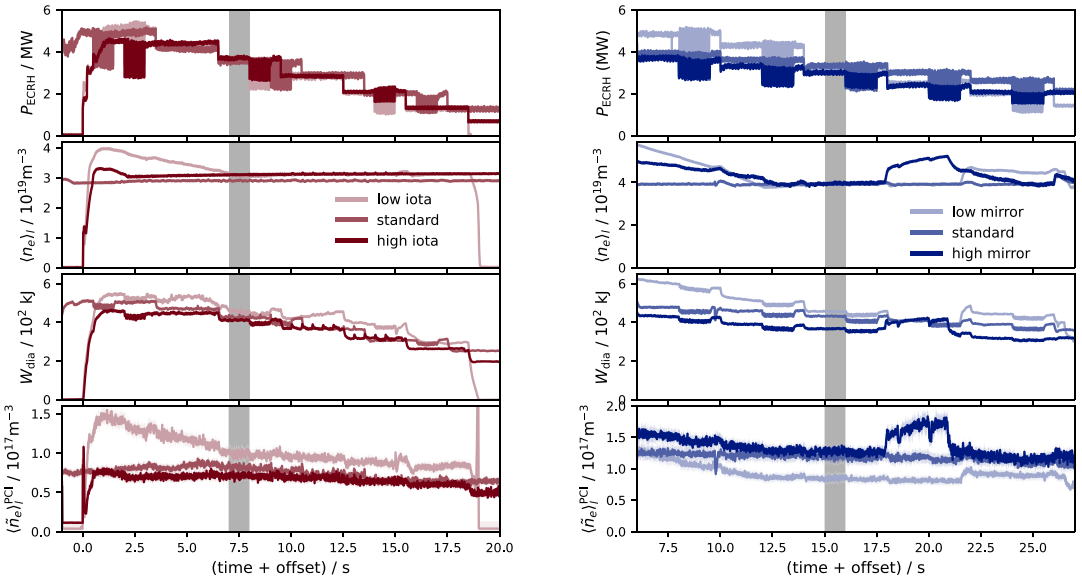

(a) Dedicated power step experiments for iota comparison.

(b) Dedicated power step experiments for mirror comparison.

Figure A1. Overview of time traces of input power, P_{ECRH}, line-averaged density, $\langle n_e \rangle_l$, diamagnetic energy, W_{dia}, and line-averaged fluctuation amplitude from PCI, $\langle \tilde{n}_e \rangle_l^{\mathrm{PCI}}$, in dedicated power step experiments.

electron cyclotron emission diagnostics. This waveform was repeated at different densities and in various magnetic configurations. In figure A1, the operation point of interest is marked as a grey shaded area. To compensate for a different timing of the power steps between the depicted experiments, an offset was applied to match time traces at the specific operation point. The bottom panel in figure A1 shows the time trace of the PCI line-integrated density fluctuation amplitude. The trend between configurations can be seen during almost all power steps. Exceptions occur due to deviations from the design density value or due to additional NBI input.

Appendix B. Linear flux tube simulations with `stella` including electron temperature drive

In the discussion in section 4, the electron temperature gradient drive has been neglected in linear simulation to highlight the ITG mode characteristics. For the sake of completeness, we present the linear growth rate spectra for the depicted cases including the electron temperature gradient and therefore all available driving mechanisms. At the given radius, electrons and ions are thermally strongly coupled and we therefore choose $a/L_{T_e} = a/L_{T_i}$ while keeping a/L_{T_i} and a/L_n unchanged. Figure B1 shows the results analogously

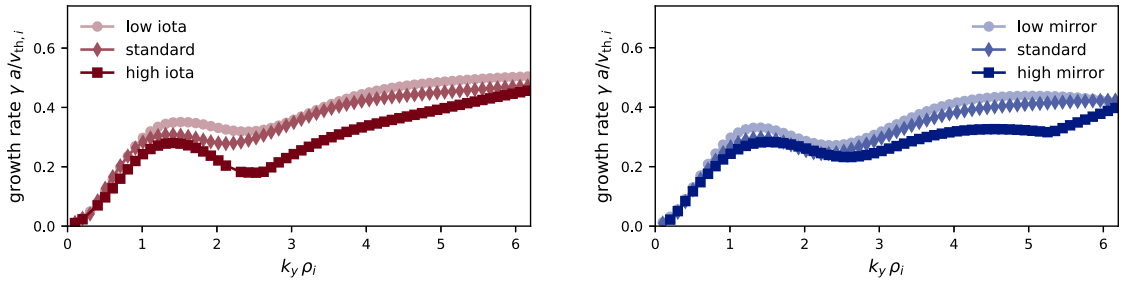

(a) Iota scan comparison. (b) Mirror scan comparison.

Figure B1. Linear gyrokinetic simulations with $a/L_{T_e} = a/L_{T_i}$ as a scan of k_y at $k_x = 0$. All other settings as described in section 4.

to figure 8. The growth rates are overall larger and increasing towards higher binormal wavenumbers. Although the depicted wavenumber range is well below the electron scale, there is an overall destabilising impact of the electron temperature gradient. However, nature of modes, the sign of their real frequency, the structure of the spectrum, i.e. separated ITG and SWITG, as well as the trend observed in the differences between magnetic configurations, do not change when including the electron temperature gradient drive.

ORCID iDs

J.-P. Bähner 0000-0002-5828-2747
L. Podavini 0000-0001-7872-3768
M. Porkolab 0000-0002-9518-4097
S.K. Hansen 0000-0002-5146-1056
A. von Stechow 0000-0003-0277-4600
S.A. Bozhenkov 0000-0003-4289-3532
O.P. Ford 0000-0002-5646-4758
G. Fuchert 0000-0002-6640-2139
A. Langenberg 0000-0002-2107-5488
N.A. Pablant 0000-0001-6617-8459
P.Zs. Pölöskei 0000-0001-7781-5599
T. Romba 0000-0002-2727-9385
A. Zocco 0000-0003-2617-3658

References

[1] Beidler C.D. *et al* 2021 Demonstration of reduced neoclassical energy transport in Wendelstein 7-X *Nature* **596** 221–6
[2] Klinger T. *et al* 2019 Overview of first Wendelstein 7-X high-performance operation *Nucl. Fusion* **59** 112004
[3] Bozhenkov S.A. *et al* 2020 High-performance plasmas after pellet injections in Wendelstein 7-X *Nucl. Fusion* **60** 066011
[4] Roberg-Clark G.T., Plunk G.G., Xanthopoulos P., Nührenberg C., Henneberg S.A. and Smith H.M. 2023 Critical gradient turbulence optimization toward a compact stellarator reactor concept *Phys. Rev. Res.* **5** L032030
[5] Hegna C.C., Terry P.W. and Faber B.J. 2018 Theory of ITG turbulent saturation in stellarators: identifying mechanisms to reduce turbulent transport *Phys. Plasmas* **25** 022511
[6] Weir G.M. *et al* 2021 Heat pulse propagation and anomalous electron heat transport measurements on the optimized stellarator W7-X *Nucl. Fusion* **61** 056001
[7] Geiger J., Beidler C.D., Feng Y., Maaßberg H., Marushchenko N.B. and Turkin Y. 2014 Physics in the magnetic configuration space of W7-X *Plasma Phys. Control. Fusion* **57** 014004
[8] Wolf R.C. *et al* (the Wendelstein 7-X Team) 2019 Performance of Wendelstein 7-X stellarator plasmas during the first divertor operation phase *Phys. Plasmas* **26** 082504
[9] Huang Z., Edlund E., Porkolab M., Bähner J.-P., Böttger L.-G., v. Sehren C., v. Stechow A. and Grulke O. 2021 The Wendelstein 7-X phase contrast imaging diagnostic *J. Instrum.* **16** 01014
[10] Hirsch M., Holzhauer E. and Hartfuss H.-J. 2006 Reflectometry for Wendelstein 7-X *Nucl. Fusion* **46** S853
[11] Windisch T. *et al* 2019 W-band doppler reflectometry at Wendelstein 7-X: Diagnostic setup and initial results *14th Intl. Reflectometry Workshop* (*Lausanne, Switzerland*) p 9 (available at: www.aug.ipp.mpg.de/IRW/IRW14/papers/207-IRW14-Windisch-paper.pdf)
[12] Edlund E.M., Porkolab M., Huang Z., Grulke O., Böttger L.-G., von Sehren C. and von Stechow A. 2018 Overview of the Wendelstein 7-X phase contrast imaging diagnostic *Rev. Sci. Instrum.* **89** 10E105
[13] Bähner J.-P. *et al* 2021 Phase contrast imaging measurements and numerical simulations of turbulent density fluctuations in gas-fuelled ECRH discharges in Wendelstein 7-X *J. Plasma Phys.* **87** 905870314
[14] Maragkoudakis E. 2025 Turbulence in Wendelstein 7-X: characterization and role in confinement *PhD Dissertation* Universidad Carlos III de Madrid
[15] Windisch T. *et al* 2018 Phased array doppler reflectometry at Wendelstein 7-X *Rev. Sci. Instrum.* **89** 10H115
[16] Beurskens M.N.A. *et al* 2021 Ion temperature clamping in Wendelstein 7-X electron cyclotron heated plasmas *Nucl. Fusion* **61** 116072
[17] Brunner K.J., Akiyama T., Hirsch M., Knauer J., Kornejew P., Kursinski B., Laqua H., Meineke J., Mora H.T. and Wolf R.C. 2018 Real-time dispersion interferometry for density feedback in fusion devices *J. Instrum.* **13** 09002
[18] Bähner J.P. 2022 Core plasma turbulence in Wendelstein 7-X *PhD Dissertation* University of Greifswald
[19] Pasch E., Beurskens M.N.A., Bozhenkov S.A., Fuchert G., Knauer J. and Wolf R.C. 2016 The Thomson scattering system at Wendelstein 7-X *Rev. Sci. Instrum.* **87** 11E729
[20] Ford O.P. *et al* 2020 Charge exchange recombination spectroscopy at Wendelstein 7-X *Rev. Sci. Instrum.* **91** 023507
[21] Langenberg A., Svensson J., Thomsen H., Marchuk O., Pablant N.A., Burhenn R. and Wolf R.C. 2016 Forward

modeling of x-ray imaging crystal spectrometers within the minerva bayesian analysis framework *Fusion Sci. Technol.* **69** 560–7
[22] Langenberg A. *et al* 2018 Prospects of x-ray imaging spectrometers for impurity transport: recent results from the stellarator Wendelstein 7-X (invited) *Rev. Sci. Instrum.* **89** 10G101
[23] Carralero D. *et al* 2020 Characterization of the radial electric field and edge velocity shear in Wendelstein 7-X *Nucl. Fusion* **60** 106019
[24] Carralero D. *et al* 2022 On the role of density fluctuations in the core turbulent transport of Wendelstein 7-X *Plasma Phys. Control. Fusion* **64** 044006
[25] González-Jerez A., García-Regaña J., Calvo I., Carralero D., Estrada T., Sánchez E. and Barnes M. (the W7-X Team) 2024 Electrostatic microturbulence in W7-X: comparison of local gyrokinetic simulations with Doppler reflectometry measurements *Nucl. Fusion* **64** 076029
[26] Fernando D.L.C.A. *et al* 2025 Validation of a comprehensive first-principles-based framework for predicting the performance of future stellarators (arXiv:2503.08943)
[27] Hirshman S.P. and Whitson J.C. 1983 Steepest-descent moment method for three-dimensional magnetohydrodynamic equilibria *Phys. Fluids* **26** 3553–68
[28] Seal S.K., Hirshman S.P., Wingen A., Wilcox R.S., Cianciosa M.R. and Unterberg E.A. 2016 Parvmec: An efficient, scalable implementation of the variational moments equilibrium code *2016 45th Int. Conf. on Parallel Processing (ICPP)* (*Philadelphia, PA, USA*) (IEEE) pp 618–27
[29] Barnes M., Parra F. and Landreman M. 2019 Stella: an operator-split, implicit-explicit δf-gyrokinetic code for general magnetic field configurations *J. Comput. Phys.* **391** 365–80
[30] D'haeseleer W.D., Hitchon W.N., Callen J.D. and Shohet J.L. 2012 *Flux Coordinates and Magnetic Field Structure: a Guide to a Fundamental Tool of Plasma Theory* (Springer)
[31] Grimm R., Dewar R. and Manickam J. 1983 Ideal MHD stability calculations in axisymmetric toroidal coordinate systems *J. Comput. Phys.* **49** 94–117
[32] Frieman E. and Chen L. 1982 Nonlinear gyrokinetic equations for low-frequency electromagnetic waves in general plasma equilibria *Phys. Fluids* **25** 502–8
[33] Helander P. *et al* 2012 Stellarator and tokamak plasmas: a comparison *Plasma Phys. Control. Fusion* **54** 124009
[34] Thienpondt H., García-Rega na J., Calvo I., Acton G. and Barnes M. 2025 Influence of the density gradient on turbulent heat transport at ion-scales: an inter-machine study with the gyrokinetic code stella *Nucl. Fusion* **65** 016062
[35] Hirose A., Elia M., Smolyakov A. and Yagi M. 2002 Short wavelength temperature gradient driven modes in tokamaks *Phys. Plasmas* **9** 1659–66
[36] Smolyakov A., Yagi M. and Kishimoto Y. 2002 Short wavelength temperature gradient driven modes in tokamak plasmas *Phys. Rev. Lett.* **89** 125005
[37] Gao Z., Sanuki H., Itoh K. and Dong J. 2003 Temperature gradient driven short wavelength modes in sheared slab plasmas *Phys. Plasmas* **10** 2831–9
[38] Rodríguez E. and Zocco A. 2025 The kinetic ion-temperature-gradient-driven instability and its localisation *J. Plasma Phys.* **91** E21
[39] Roberg-Clark G., Xanthopoulos P. and Plunk G. 2024 Reduction of electrostatic turbulence in a quasi-helically symmetric stellarator via critical gradient optimization *J. Plasma Phys.* **90** 175900301
[40] Helander P. 2014 Theory of plasma confinement in non-axisymmetric magnetic fields *Rep. Prog. Phys.* **77** 087001
[41] Waltz R. and Boozer A. 1993 Local shear in general magnetic stellarator geometry *Phys. Fluids B* **5** 2201–5
[42] Plunk G., Helander P., Xanthopoulos P. and Connor J. 2014 Collisionless microinstabilities in stellarators. III. The ion-temperature-gradient mode *Phys. Plasmas* **21** 032112
[43] Podavini L., Zocco A., García-Regaña J.M., Barnes M., Parra F.I., Mishchenko A. and Helander P. 2024 Ion-temperature- and density-gradient-driven instabilities and turbulence in Wendelstein 7-X close to the stability threshold *J. Plasma Phys.* **90** 905900414
[44] Plunk G., Connor J. and Helander P. 2017 Collisionless microinstabilities in stellarators. Part 4. The ion-driven trapped-electron mode *J. Plasma Phys.* **83** 715830404
[45] Proll J.H.E., Plunk G.G., Faber B.J., Görler T., Helander P., McKinney I.J., Pueschel M.J., Smith H.M. and Xanthopoulos P. 2022 Turbulence mitigation in maximum-J stellarators with electron-density gradient *J. Plasma Phys.* **88** 905880112
[46] Costello P. and Plunk G. 2025 Energetic bounds on gyrokinetic instabilities. Part 4. Bounce-averaged electrons *J. Plasma Phys.* **91** E12
[47] Proll J.H.E., Helander P., Connor J.W. and Plunk G.G. 2012 Resilience of quasiisodynamic stellarators against trapped-particle instabilities *Phys. Rev. Lett.* **108** 245002
[48] Proll J.H.E., Xanthopoulos P. and Helander P. 2013 Collisionless microinstabilities in stellarators. II. Numerical simulations *Phys. Plasmas* **20** 122506
[49] Helander P., Proll J.H.E. and Plunk G.G. 2013 Collisionless microinstabilities in stellarators. I. Analytical theory of trapped-particle modes *Phys. Plasmas* **20** 122505
[50] Alcusón J., Xanthopoulos P., Plunk G., Helander P., Wilms F., Turkin Y., Stechow A.V. and Grulke O. 2020 Suppression of electrostatic micro-instabilities in maximum-*J* stellarators *Plasma Phys. Control. Fusion* **62** 035005
[51] Maurer M., Bañón Navarro A., Dannert T., Restelli M., Hindenlang F., Görler T., Told D., Jarema D., Merlo G. and Jenko F. 2020 GENE-3D: a global gyrokinetic turbulence code for stellarators *J. Comput. Phys.* **420** 109694
[52] Wilms F., Navarro A.B., Merlo G., Leppin L., Görler T., Dannert T., Hindenlang F. and Jenko F. 2021 Global electromagnetic turbulence simulations of W7-X-like plasmas with GENE-3D *J. Plasma Phys.* **87** 905870604
[53] Navarro A.B., Siena A.D., Velasco J.L., Wilms F., Merlo G., Windisch T., LoDestro L.L., Parker J.B. and Jenko F. 2023 First-principles based plasma profile predictions for optimized stellarators *Nucl. Fusion* **63** 054003
[54] García-Regaña J., Calvo I., Parra F. and Thienpondt H. 2024 Reduction or enhancement of stellarator turbulence by impurities *Phys. Rev. Lett.* **133** 105101